Three-dimensional image reconstruction of radiation-sensitive samples with x-ray diffraction microscopy

Chien-Chun Chen,[1,2] Chien-Hung Lu,[1,4] D. Chien,[3] Jianwei Miao,[2] and T. K. Lee[1,*]

[1]*Institute of Physics, Academia Sinica, Nankang, Taipei 11529, Taiwan*

[2]*Department of Physics and Astronomy and California NanoSystems Institute, University of California Los Angeles, Los Angeles, California 90095, USA*

[3]*Department of Mathematics, California State University San Marcos, San Marcos, California 92096, USA*

[4]*Department of Electrical Engineering, Princeton University, Princeton, New Jersey 08544, USA*

(Received 14 March 2011; published 7 July 2011)

Coherent diffraction microscopy determines the three-dimensional (3D) structure of a noncrystalline sample by acquiring a set of diffraction patterns at multiple sample orientations. In order to achieve a high spatial resolution, it usually requires a large number of diffraction patterns with small increments of tilt angles. However, this is not easily attainable for biological or other radiation-sensitive samples due to the radiation damage issue. With the constraint that only a limited number of diffraction patterns is available, a new method is proposed to optimize the effect of these data for three-dimensional image reconstruction. The method combines the concepts of selecting angles with a constant slope increment, the pseudopolar Fourier transform, and the guided hybrid input-output method for direct 3D phase retrieval. Based on simulated and experimental data, it is shown that the proposed method has a better accuracy than some existing three-dimensional image reconstruction techniques. The method is also examined for its stability and consistency by reducing data points used for image reconstruction. The relationship between the number of diffraction patterns used and the accuracy of the reconstructed images is also studied.

DOI: 10.1103/PhysRevB.84.024112 PACS number(s): 42.30.Rx, 61.05.cc

Since its first demonstration in 1999,[1] coherent diffraction microscopy (CDM), also termed coherent diffractive imaging or lensless imaging, has been advancing rapidly by using synchrotron radiation,[2–22] electrons,[23–29] x-ray free electron lasers,[30–32] high-harmonic generation, and table-top soft x-ray lasers.[33–35] In CDM, the diffraction pattern of a noncrystalline specimen or a nanocrystal is measured and then directly phased to obtain an image. The well-known phase problem is solved by using the oversampling method[36] in combination with the iterative algorithms.[37–41] One of the important applications of CDM is its ability to perform quantitative three-dimensional (3D) imaging of noncrystalline specimens and nanocrystals by using coherent x rays.[3,5,9–12,14,19,20,52] While ankylography can potentially be applied to determine the 3D structure of small objects,[42] currently the established scheme for 3D structure determination of general samples is implemented by acquiring a set of diffraction patterns at multiple sample orientations.[3,5,9–12,14,19,20,23,43] To map out the strain field inside nanocrystals, the set of diffraction patterns can be directly assembled into a 3D pattern and then phased to obtain the 3D shape and the strain field of the nanocrystals.[5,10,14] However, to obtain the 3D electron densities of noncrystalline samples, the diffraction patterns are measured on the polar grid while the reconstructed 3D image has to be sampled on the Cartesian grid.[3,9,11,12,14,19,20,23] The coordinate transformation from the polar to Cartesian grids is a complicated process and the implementation scheme of this process directly affects the quality of the final 3D reconstruction.

To date, two types of 3D reconstruction approaches have been developed. One is achieved by interpolating a 3D diffraction pattern from the set of the two-dimensional (2D) patterns and then performing direct 3D phase retrieval.[3,12,14,19,20] The other is to phase each individual 2D diffraction pattern and then compute 3D reconstruction from 2D projection images.[11,43] Although both reconstruction methods have been applied to perform 3D structure determination of inorganic and biological samples, each has its intrinsic limitations.

In the first approach, the interpolation process in Fourier space is usually unfavorable as the signal variation in Fourier space is much larger than that in real space. Therefore, the most challenged issue is to keep the fidelity during coordinate transformation, especially in the central region. Intensities within the central area could usually vary by several orders of magnitude. Simple interpolation methods, such as average, linear, or cubic interpolation, and gridding method may not work well. In addition, the aforementioned transformation between polar grids and Cartesian grids also requires a significant amount of interpolation. Furthermore, the errors of interpolation rapidly increase when experiments cannot provide data at the central pixel due to a beam stop or at large angles within a $\pm 20^{\circ}$ wedge due to the missing wedge problem. In addition, for biological or radiation-sensitive specimens, the number of measured 2D diffraction patterns is limited due to the radiation damage problem.[44,45] The heavy dependence on interpolation is a cause for concern.

In the second approach, phase retrieval is performed on each individual 2D diffraction pattern and then each 2D projection image needs to be aligned with the common rotation axis. Although the equally sloped tomographic (EST) reconstruction has been developed to reduce the errors in tomography and has been demonstrated to enhance the image resolution, quality, and contrast relative to the conventional tomographic reconstructions,[46–49] a feasible alignment method with high accuracy is still needed. Even though a method has recently been developed to improve the alignment accuracy,[50] noises in the experimental data may still cause errors in

alignment that will affect the quality of the reconstructed 3D images. From the point of view of optimization, this approach is like a local optimization that we optimize the phase retrieval problem only for each individual 2D projection. The retrieved phases from diffraction patterns at different angles are not necessarily consistent, while the first approach optimizes the whole 3D phases together and may obtain a more consistent image.

Here, we develop a new method that takes advantage of both the EST method and the direct 3D phase-retrieval method to optimize the image reconstruction from a limited number of diffraction patterns. The main idea of the proposed method is to first determine the intensities at as many Cartesian grids as possible and as accurately as possible. In addition, we aim to use only a relatively limited number of projections with a large angular increment between successive projections. The idea proposed by the EST method[46–49] is clearly a good choice to begin this approach as it takes projections with a constant slope increment instead of a constant angular increment. The EST method uses the idea of pseudopolar Fourier transform (PPFT) to maximize the number of common grids between pseudopolar and Cartesian coordinates.[51] Basically, the PPFT is a combination of Fourier transform (FT) along the direction of rotation axis and fractional FT in the perpendicular direction. For example, let us consider how fractional FT works between polar and Cartesian grids at the angle 45°. As we pick up the line at 45°, the distance of each two Cartesian grids is $\sqrt{2}$ times larger than polar grids. Hence, by re-sampling the intensities at a larger frequency interval, it would be theoretically possible to calculate the correct intensities on those Cartesian grids. Thus by using the PPFT, our proposed method could obtain correct intensities at many Cartesian grids without relying on interpolation or optimization as other approaches.[3,12,14] By using these grids as our basic input we are able to obtain more accurate interpolation for missing intensity data on other Cartesian grids. Furthermore, we have minimized the number of grids to be interpolated. Once the intensities of all 3D Cartesian grids are determined we then proceed to retrieve the phases with the guided HIO method (GHIO).[39] This approach not only avoids the alignment problem encountered in the EST method it also improves the reconstruction accuracy with more grids transformed from experimental data directly and fewer numbers of grids for interpolation. The method is also effective for data with a missing center and missing wedge. Results from a phantom model and an experimental data set of the GaN-Ga_2O_3 nanoparticle[9,11] are compared favorably with the existing 3D image reconstruction techniques. In the final part of this paper, the relation between the number of projections and the desired resolution is also studied. The accuracy and robustness of the method is carefully evaluated by deliberately removing projection data at some angles in order to check the consistency among the reconstruction and missing data.

Now we shall present the detailed steps of the proposed method. First, for each 2D diffraction pattern, we have to solve the missing center problem so that we can perform the inverse Fourier transform to obtain the density-density correlation function or the Patterson function. After the Patterson function at a particular projection angle is obtained, we apply the PPFT and calculate the intensities on pseudopolar grids, which will be used to obtain the intensities on Cartesian grids. To recover the missing data at the center for each projection we could just treat them as unknown variables using an iterative method such as the HIO algorithm[37] just as the usual method of retrieving phases for each 2D diffraction pattern. However, that will require a substantial amount of computation and it is not as accurate as we desire. Actually, we do not really need a very precise determination of intensities at these missing centers to obtain accurate intensities at the pseudopolar grids which are outside of the missing centers. In Appendix we provide a simple theorem to show this is actually possible. All we really need is to obtain a simulated band-limited Patterson function that reproduces accurately the measured diffraction intensities outside the missing center. This particular Patterson function could have a size much larger than the real sample. It has the advantage of fast convergence while keeping a high accuracy of intensities outside the missing center. Such a goal could be easily obtained by using the HIO algorithm as both intensities and the Patterson function are real. Those somewhat inaccurate intensities in the missing centers will be treated as variables in later calculation to retrieve 3D phases and to reconstruct the images.

In order to enhance the accuracy of the coordinate transformation process, we select the angles with a constant slope increment as in EST. For example, in the case with an angle of $\tan^{-1}1/16$, we can calculate very accurately experimental intensities at Cartesian grids with coordinates (16,1), (32,2), . . . , etc. through the PPFFT. In the case with an angle of $\tan^{-1}1/8$, we can obtain experimental intensities with Cartesian grids (8,1), (16,2), (24,3), (32,4), . . . , etc. In this way we obtain accurate intensities at a significant number of Cartesian grids. However, it is easy to see there are still many grid points without intensity values, including the points inside the missing wedge and the missing central region. We will use interpolation to determine intensities for some of these grids and leave the rest as variables. While a number of interpolation methods exist, we found the best approach is to interpolate the intensities on Cartesian grids from those on pseudopolar grids in the small k region. Since the intensities on pseudopolar grids are denser than Cartesian grids in the small k region, it is possible to achieve accurate interpolation. For the large k region, we simply use the nearest neighboring interpolation to obtain some of data points on the Cartesian grids if these points are close to the pseudopolar grids; otherwise, they will be treated as variables to be determined. Then we use the GHIO algorithm to recover the phases and the 3D electron densities by treating all the intensity points in the missing center, missing wedge, and those large k grids without data as variables to be determined by the iterative process. Of course, we need to have a large enough oversampling ratio to make sure the set of known data in real space and Fourier space is much larger than the set of unknown variables to be determined.

To test the proposed method, we first perform 3D image reconstruction on a phantom model. The 3D model, with a size of $51 \times 51 \times 51$ voxels and a uniform charge density of 5, consists of 16 alphabetical posts and the central layer (i.e., 26th layer) is set to be an empty gap. Figures 1(a)–1(c) show the iso-surface rendering, the 25th layer, and the projection at 90° of the model, respectively. Fifty-three successive diffraction patterns are computed from the model with an equal slope increment of 1/16 and an angular range from

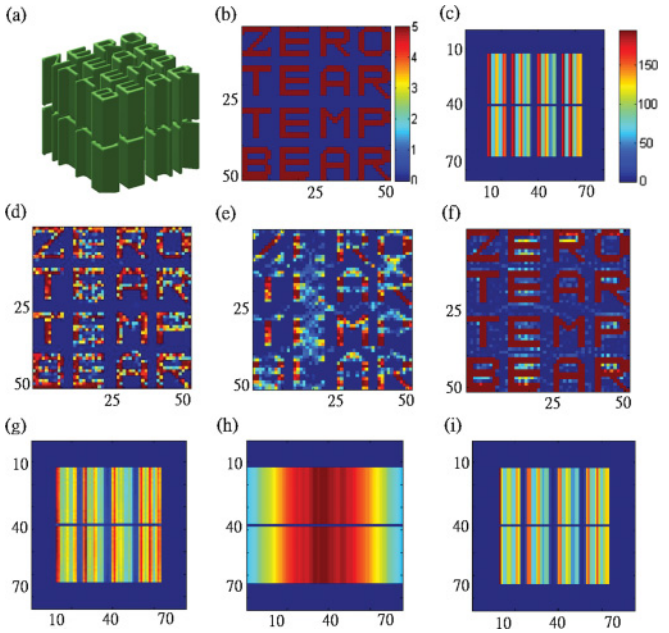

FIG. 1. (Color online) (a) Iso-surface rendering of the 3D model. (b) The 25th layer of the model. (c) Projection at 90°of the model. (d)–(f) The 25th layer of 3D image reconstructed by our method, FBP, and EST, respectively. (g)–(i) Projections of the 3D reconstructed image at 90° by our method, FBP, and EST, respectively.

$-69.44°$ to $+69.44°$. The size of each diffraction pattern is 201×201 pixels with a missing center of 7×7 pixels. We first compare the proposed method to two tomographic reconstruction techniques, filtered back propagation (FBP) and EST. Figure 1(d) shows the result obtained by the proposed method. In the implementations of FBP and EST, we assume the 53 projections are exactly phased and aligned. With such prerequisites, the results are shown in Figs. 1(e) and 1(f), respectively.

To perform a quantitative comparison, we use two error metrics. As in x-ray crystallography, the E_R in real space is defined as

$$E_R = \frac{\sum_{r\in S} ||g(r)| - |f(r)||}{\sum_{r\in S} |f(r)|}, \quad (1)$$

where $g(r)$, $f(r)$, and S are the reconstructed image, the exact solution, and the boundary of the image.

The E_F in Fourier space is defined as

$$E_F = \frac{\sum_{k\in D} ||H(k)| - |F(k)||}{\sum_{k\in D} |F(k)|}, \quad (2)$$

where $|H(k)|$, $|F(k)|$, and D represent the calculated Fourier modulus, the measured Fourier modulus, and the extent of the diffraction pattern, respectively. The E_R of Figs. 1(d)–1(f) are 0.381, 0.740, and 0.178 for our method, FBP, and EST, respectively. Our method has a smaller error than FBP, but a larger error than EST. This is because we have assumed that the 2D projections of EST are exactly reconstructed and aligned, hence the projections provide exact phase information in EST. If this assumption does not hold, the reconstruction error in EST could be larger than that of our method as we will show it below with experimental data. Another important test of our method is to project the reconstructed 3D image back to the missing wedge region. Figures 1(g)–1(i) show the projections at 90° from the 3D reconstructed image by our method, FBP, and EST, respectively. Apparently, both EST and our method reconstruct the image at this angle correctly, although EST gives a better accuracy. We also compute the E_Fs of our 3D method, FBP, and EST for the projections at 90°, which are 0.18, 0.62, and 0.12, respectively. This demonstrates the proposed method is capable of reproducing the images quite accurately even in the region without diffraction data.

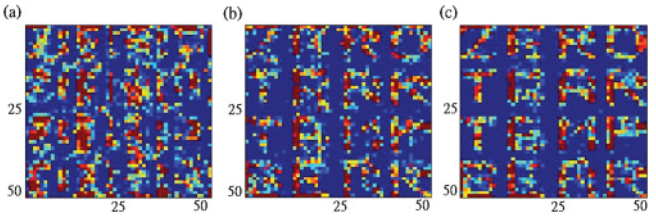

FIG. 2. (Color online) The 25th layer of the reconstructed 3D model by using (a) nearest neighbor interpolation and averaging (method A), (b) the re-weighting interpolation (method B), and (c) the MATLAB grid data function (method C). The indices on the left and below the panels denote the pixel number. The reconstruction of our method is shown in Fig. 1(d).

We further examine the interpolation method used here with three other interpolation methods used before. In the interpolation method A, the intensities on the Cartesian grids are set to be the same as the nearest neighbor points on the polar grids. If more than one point contributes to a given voxel, those points are averaged to determine the voxel value.[12,19] In method B the intensities on Cartesian grids are determined by weighting the ratio of overlap region between the polar and Cartesian grid voxels.[3,20] In method C, the grid data function in MATLAB is used for interpolation. Figures 2(a)–2(c) show the 25th layer of the reconstructed images by methods A, B, and C, respectively, and their corresponding E_Rs are 1.230, 0.779, and 0.626, respectively. These errors are much larger than that of our method (0.381) shown in Fig. 1(d). Table I lists E_Fs computed in three separated regions for A, B, C, and our approach. Region 1 represents those common points between the pseudopolar and Cartesian grids. Region 2 represents the small k region or the central 129×129 pixels. All the other grid points obtained by interpolation are defined as Region 3. Our approach enables one to retrieve the correct values on the common grids so that the E_F in Region 1 is extremely small. Furthermore, our approach performs a better interpolation in Regions 2 and 3 than the other three interpolation methods. By taking the advantage of having denser grids in the small k region and avoiding extensive interpolation in large k regions, we obtain more accurate results.

To test the proposed method more rigorously, we perform a 3D reconstruction of an experimental data set and then compare it with the FBP and EST reconstructions. The experimental data set consists of 27 2D diffraction patterns acquired at a constant slope increments of 1/8 from a GaN-Ga_2O_3 nanoparticle.[9,11] From the 3D images reconstructed by FBP, EST, and our method, we compute the corresponding E_Fs at each angle for three different methods, shown in Table II.

TABLE I. The E_Fs are calculated within different interpolated regions by using methods A, B, C, and our approach. Please refer to the text for the definition of Regions 1, 2, and 3.

	Method A	Method B	Method C	Our approach
Region 1	0.068	0.059	0.022	6.5×10^{-5}
Region 2	0.150	0.108	0.088	0.068
Region 3	0.169	0.123	0.104	0.084

Although the size of each original diffraction pattern is 800 × 800 pixels, we chose the central 201 × 201 pixel diffraction pattern for the comparison purpose as these intensities have higher signal-to-noise ratios. Table II shows that our method improves accuracy of 150% over FBP and of 80% over EST. Although FBP performs well at smaller angles, its error increases rapidly at larger angles due to a large portion of the missing intensity points in that region.

Figures 3(a) and 3(d) show the projections at 51° and 90° from the 3D reconstructed image by our method. The corresponding projections from the 3D reconstructed images by EST and FBP are shown in Figs. 3(b), 3(e), 3(c) and 3(f), respectively. Since there are no experimental data available for these two angles, the E_F or E_R cannot be computed in these cases. However, we know the nanoparticle is a band-limited object and confined within a suitable support. Only the images obtained by the proposed method and EST seem to have the proper shape. If we examine more carefully the projection at 90°, the EST image seems to have densities aggregated around the edge even though the loose support does not crop the sample, which are most likely artifacts. In addition, FBP makes the reconstructed image look "fatter" and the object is surrounded by some fuzzy density which is likely caused by the missing wedge problem.

To further study the proposed method, we reconstruct the 3D image from the experimental data set by using a smaller number of diffraction patterns. We first omit the 2D diffraction pattern at ±69.44° and perform 3D image reconstruction only

TABLE II. E_Fs corresponding to experimental amplitudes within the region of central 201 × 201 pixels are calculated at each angle. The sequential columns from left to right are E_Fs of the 3D reconstructed images by FBP, EST, and our method.

Angle	FBP	EST	Our	Angle	FBP	EST	Our
0°	0.125	0.157	0.075	−7.13°	0.128	0.130	0.099
7.13°	0.114	0.127	0.055	−14.04°	0.144	0.138	0.096
14.04°	0.111	0.117	0.061	−20.56°	0.160	0.158	0.101
20.56°	0.118	0.114	0.057	−26.57°	0.177	0.152	0.085
26.57°	0.132	0.121	0.068	−32.01°	0.209	0.168	0.084
32.01°	0.196	0.128	0.081	−36.87°	0.221	0.178	0.089
36.87°	0.292	0.157	0.140	−41.19°	0.298	0.192	0.082
41.19°	0.267	0.171	0.089	−45°	0.333	0.190	0.089
45°	0.299	0.174	0.082	−48.81°	0.310	0.169	0.092
48.81°	0.296	0.156	0.061	−53.13°	0.276	0.158	0.088
53.13°	0.254	0.155	0.075	−57.99°	0.212	0.148	0.091
57.99°	0.213	0.151	0.067	−63.43°	0.169	0.175	0.090
63.43°	0.223	0.109	0.068	−69.44°	0.212	0.168	0.102
69.44°	0.265	0.107	0.091	Average	0.213	0.151	0.084

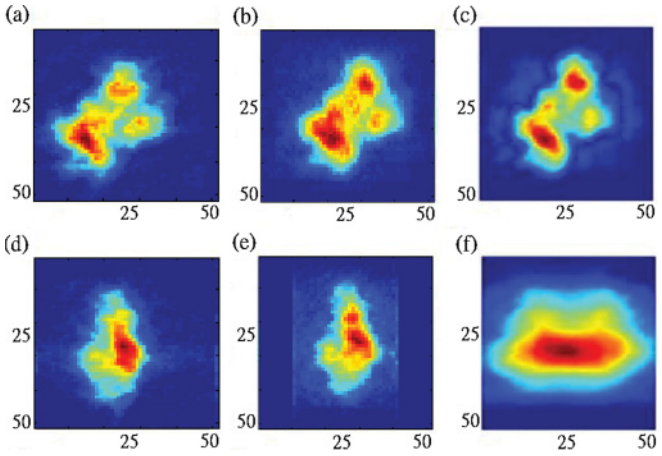

FIG. 3. (Color online) The projections at 51° and 90° from the 3D images reconstructed by (a) and (d) our method; (b) and (e) EST; and (c) and (f) FBP. The color represents the density distribution and the indices on the left and below the panels are the pixel number. The scale of color is same as in Fig. 4.

from 25 diffraction patterns. We then compare the projection images from the 3D reconstructed image with the 2D images directly reconstructed from the diffraction patterns by 2D GHIO.[39] Figures 4(a) and 4(b) show two projection images from the 3D reconstructed image at ±69.44°, which are in good agreement with the 2D GHIO reconstructed images, shown in Figs. 4(c) and 4(d). Quantitative comparisons indicate that the E_Fs of Figs. 4(a) and 4(b) are 0.111 and 0.106, and the E_F of Figs. 4(c) and 4(d) are 0.066 and 0.121, respectively. The E_Fs of Figs. 4(a) and 4(b) are also consistent with those of

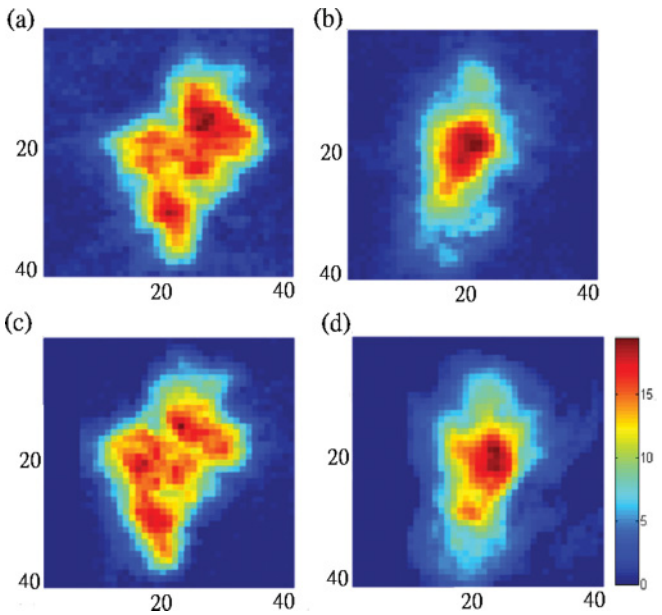

FIG. 4. (Color online) (a) and (b) Projective images from a 3D image reconstructed by our method at ±69.44°. (c) and (d) 2D reconstructed images from experimental diffraction patterns at ±69.44° by the 2D GHIO algorithm. The color represents the density distribution and the indices on the left and below the panels are the pixel number.

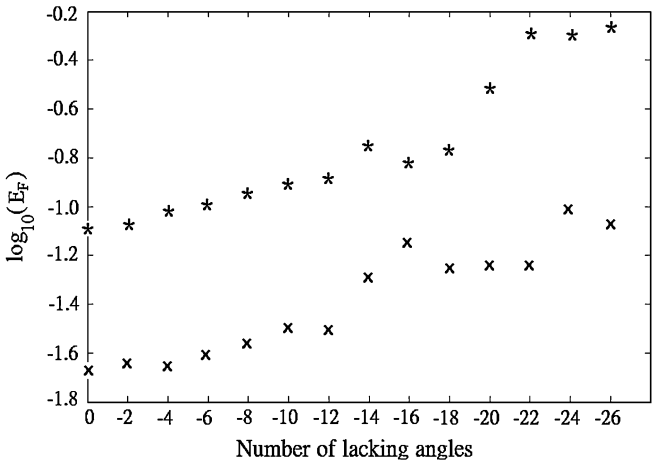

FIG. 5. The average E_Fs in logarithmic scale as a function of the number of removed projections. The projections are removed by following the sequence of $\pm 69.44^\circ$, $\pm 63.43^\circ$, $\pm 57.99^\circ, \ldots,$ $\pm 14.04^\circ$ and finally $\pm 7.13^\circ$. For example, "-2" in the x axis denotes projections at $\pm 69.44^\circ$ are removed and so on. The phantom model is labeled with crosses and the GaN-Ga_2O_3 case labeled with stars.

using the full data set, shown in Table II, where E_Fs are 0.091 and 0.102 for $\pm 69.44^\circ$, respectively. We have further tested our method by removing another pair of diffraction patterns at $\pm 41.19^\circ$. The 3D image reconstructed only from 23 2D diffraction patterns has the similar quality as that of using the full data set.

A conclusion can be drawn from these independent tests that even if there are missing data at high angles and there exists a fewer number of 2D diffraction patterns, the proposed method can still retrieve the missing data with a reasonable accuracy. Hence if we can tolerate somewhat less resolutions, we may reduce the number of projections needed from experimental measurements. Below we will study the relationship between the number of projections used for our method and the error in the reconstructed images.

We now apply the proposed method to reconstruct the 3D images by successively reducing the number of the projections. First we consider the phantom model shown in Fig. 1. Instead of using all 53 2D diffraction patterns, we now remove sequentially diffraction patterns with rotation angles of $\pm 69.44^\circ$, $\pm 66.37^\circ$, $\pm 63.43^\circ, \ldots,$ etc. Figure 5 shows the average E_F plotted in a logarithmic scale as a function of the number of removed projections (labeled as crosses), where E_F is computed from the central 51×51 pixels. The average E_F only increases from 0.22 to 0.31 as we reduce the number of projections from 53 to 41 where the maximum rotation angle is only 53.13° in the latter case. In the reconstructed image using just 41 projections, letters B and E are barely recognizable but other letters are still visible. The resolution in this case is about 3 pixels versus 2 pixels for the reconstruction of the full data set. For the GaN-Ga_2O_3 case, there are only 27 experimental projections. During the reconstructions we also sequentially remove projections with rotation angles of $\pm 69.44^\circ$, $\pm 63.43^\circ$, $\pm 57.99^\circ, \ldots,$ etc., so that the number of projections decreases from 27 to 1. The average E_Fs is plotted as a function of a number of removed projections, shown in Fig. 5 (labeled as stars). The results indicate that we can reduce the number of projections to about 15 with a maximum angle of 41.19° while the error only increases slightly.

In summary, we have developed a new method to reconstruct a 3D image directly from measured diffraction intensities. Taking into account the constraint that only a relatively small number of projections may be acquired from radiation-sensitive samples and also the fact that there are missing data due to the missing center and wedge problem, the proposed method aims to optimize the effect of these limited data in 3D image reconstructions. By choosing the rotational angles in a constant slope increment that will have a maximum number of common grids between pseudopolar and Cartesian coordinates, the proposed method assembles a 3D diffraction pattern in Cartesian grids from a set of 2D diffraction patterns in pseudopolar grid, and then computes a 3D image by using the GHIO algorithm. In this approach the uncertainty associated with alignment which has plagued the previous EST method is circumvented. Not only better resolutions but also smaller errors have been achieved in comparison with the existing 3D image reconstruction techniques. Finally, we have demonstrated that the proposed method enables one to perform reasonably good reconstructions even with a small number of projections. It is anticipated that the proposed method will find applications in 3D image reconstructions using coherent diffraction microscopy. The method will be especially beneficial for 3D imaging of radiation-sensitive and biological specimens.

We thank C. Song, Y. Nishino, and Y. Kohmura for data acquisition and data analysis of the GaN-Ga_2O_3 nanoparticle and S. Risbud for providing the sample. This work was supported in part by the US Department of Energy, Basic Energy Sciences (Grant No. DE-FG02-06ER46276), the US National Institutes of Health (Grant No. GM081409-01A1), and the Taiwan National Science Council (Grant No. 98-2112-M-001-017-MY3). Use of the RIKEN beamline (BL29XUL) at SPring-8 was supported by RIKEN.

APPENDIX

The lost intensities in the central region prohibit us from obtaining correct Patterson function by directly applying inverse fast Fourier transform (IFFT). Without a Patterson function, we are not able to apply PPFT to calculate intensities on pseudopolar grids.[46] Actually for our method we do not need an accurate representation of intensities within the missing central region; what we really want is to find a band-limited Patterson function that could reproduce accurately the measured intensities on the Cartesian grids outside the missing central region. We prove below a theorem that shows if we can get correct values for discrete Cartesian grids outside the central region, then we have also obtained an accurate representation of the continuous function of the intensities outside the region. This is necessary to guarantee intensities on pseudopolar grids outside the missing central region are also accurate. To get the simulated Patterson function with accurate Cartesian grids outside the central region, we use the well-known iterative HIO method using the measured intensities as input and missing central region as variables. Since both intensities and the Patterson function are real, it is

quite straightforward to find converged solutions. In fact, based on the theorem presented below, we may enlarge the size of the simulated Patterson function as long as the requirement that the sampling frequency be finer than or equal to the Nyquist frequency is satisfied. Usually the larger the size with more variables to adjust, the easier it is to get a converged and higher accuracy result. This is an important advantage when we proceed to do PPFT.

Before we prove the statement, we shall start with Shannon's theorem, if a real function $P(r)$ is band limited with size L, it is possible to retrieve the function $I(k)$ in frequency or Fourier space domain by only sampling the function at discrete k value $I[nK]$, provided that $K < 1/L$ where $1/L$ is the Nyquist frequency. Here n is an integer. One of the consequences of the theorem is that if two band-limited functions have identical $I[nK]$ for all n, then the two functions are identical, and so are their Fourier transform $I(k)$ for continuous k values. We shall take one step further with the following theorem.

Theorem 1. Two distinct band-limited functions $P_1(r)$ and $P_2(r)$ with size L_1 and L_2 have their discrete Fourier transform $I_1[nK]$ and $I_2[nK]$, where n is any integer, $K < 1/L_1$ and $K < 1/L_2$, If $I_2[nK] = I_1[nK]$ for all $|n| > |m|$ where the integer m represents the size of the central region, then the function $I_1(k) = I_2(k)$ for all continuous $|k| > |mK|$.

Proof. Since we have $I_1(k)$ and $I_2(k)$, we can define a new continuous function $I_3(k)$ as

$$I_3(k) = \begin{cases} I_1(k), & \text{if } k \in BS \\ I_2(k), & \text{if } k \notin BS, \end{cases} \tag{A1}$$

where BS, the beam stop, is the region within k less than or equal to $|mK|$. Thus we can also deduce the discrete sampling of $I_3(k)$ from Eq. (3), as $I_3[nK]$ where

$$I_3[nK] = \begin{cases} I_1[nK], & \text{if } nK \in BS \\ I_2[nK], & \text{if } nK \notin BS. \end{cases} \tag{A2}$$

Since $I_2[nK] = I_1[nK]$ for all $|n| > |m|$ (i.e., sampled intensities outside of the BS region), $I_3[nK] = I_1[nK]$ for all nK. Based on Shannon's theorem, this would imply $I_3(k) = I_1(k)$ for all k. Using Eq. (3), we obtain $I_2(k) = I_1(k)$ for all $|k| > |mK|$. ■

The main consequence of the above theorem is that we do not have to find the correct Patterson function in the missing central region, but to find a simulated band-limited Patterson function that can produce discrete Cartesian grids, consequently continuous k, correctly outside the central region. Furthermore, to apply the theorem which is valid for k values extended to infinity, we have to make an assumption that the intensities outside of the measured diffraction pattern are negligible.

*tklee@phys.sinica.edu.tw

[1] J. Miao, P. Charalambous, J. Kirz, and D. Sayre, Nature (London) **400**, 342 (1999).

[2] I. K. Robinson, I. A. Vartanyants, G. J. Williams, M. A. Pfeifer, and J. A. Pitney, Phys. Rev. Lett. **87**, 195505 (2001).

[3] J. Miao, T. Ishikawa, B. Johnson, E. H. Anderson, B. Lai, and K. O. Hodgson, Phys. Rev. Lett. **89**, 088303 (2002).

[4] J. Miao, K. O. Hodgson, T. Ishikawa, C. A. Larabell, M. A. LeGros, and Y. Nishino, Proc. Natl. Acad. Sci. USA **100**, 110 (2003).

[5] G. J. Williams, M. A. Pfeifer, I. A. Vartanyants, and I. K. Robinson, Phys. Rev. Lett. **90**, 175501 (2003).

[6] S. Marchesini, H. He, H. N. Chapman, S. P. Hau-Riege, A. Noy, M. R. Howells, U. Weierstall, and J. C. H. Spence, Phys. Rev. B **68**, 140101(R) (2003).

[7] K. A. Nugent, A. G. Peele, H. N. Chapman, and A. P. Mancuso, Phys. Rev. Lett. **91**, 203902 (2003).

[8] D. Shapiro *et al*., Proc. Natl. Acad. Sci. USA **102**, 15343 (2005).

[9] J. Miao, Y. Nishino, Y. Kohmura, B. Johnson, C. Song, S. H. Risbud, and T. Ishikawa, Phys. Rev. Lett. **95**, 085503 (2005).

[10] M. A. Pfeifer, G. J. Williams, I. A. Vartanyants, R. Harder, and I. K. Robinson, Nature (London) **442**, 63 (2006).

[11] J. Miao, C. C. Chen, C. Song, Y. Nishino, Y. Kohmura, T. Ishikawa, D. Ramunno-Johnson, T. K. Lee, and S. H. Risbud, Phys. Rev. Lett. **97**, 215503 (2006).

[12] H. N. Chapman *et al*., J. Opt. Soc. Am. A **23**, 1179 (2006).

[13] G. J. Williams, H. M. Quiney, B. B. Dhal, C. Q. Tran, K. A. Nugent, A. G. Peele, D. Paterson, and M. D. deJonge, Phys. Rev. Lett. **97**, 025506 (2006).

[14] I. K. Robinson and J. Miao, MRS Bull. **29**, 177 (2004).

[15] B. Abbey *et al*., Nat. Phys. **4**, 394 (2008).

[16] H. Jiang, D. Ramunno-Johnson, C. Song, B. Amirbekian, Y. Kohmura, Y. Nishino, Y. Takahashi, T. Ishikawa, and J. Miao, Phys. Rev. Lett. **100**, 038103 (2008).

[17] P. Thibault *et al*., Science **321**, 379 (2008).

[18] C. Song, H. Jiang, A. Mancuso, B. Amirbekian, L. Peng, R. Sun, S. S. Shah, Z. H. Zhou, T. Ishikawa, and J. Miao, Phys. Rev. Lett. **101**, 158101 (2008).

[19] A. Barty *et al*., Phys. Rev. Lett. **101**, 055501 (2008).

[20] Y. Nishino, Y. Takahashi, N. Imamoto, T. Ishikawa, and K. Maeshima, Phys. Rev. Lett. **102**, 018101 (2009).

[21] X. Huang *et al*., Phys. Rev. Lett. **103**, 198101 (2009).

[22] E. Lima, L. Wiegart, P. Pernot, M. Howells, J. Timmins, F. Zontone, and A. Madsen, Phys. Rev. Lett. **103**, 198102 (2009).

[23] J. Miao, T. Ohsuna, O. Terasaki, K. O. Hodgson, and M. A. O'Keefe, Phys. Rev. Lett. **89**, 155502 (2002).

[24] J. M. Zuo, I. Vartanyants, M. Gao, R. Zhang, and L. A. Nagahara, Science **300**, 1419 (2003).

[25] J. C. H. Spence, U. Weierstall, and M. R. Howells, Philos. Trans. R. Soc. London A **360**, 875 (2002).

[26] O. Kamimura, K. Kawahara, T. Doi, T. Dobashi, T. Abe, and K. Gohara, Appl. Phys. Lett. **92**, 024106 (2008).

[27] S. Morishita, J. Yamasaki, K. Nakamura, T. Kato, and N. Tanaka, Appl. Phys. Lett. **93**, 183103 (2008).

[28] W. J. Huang, J. M. Zuo, B. Jiang, K. W. Kwon, and M. Shim, Nat. Phys. **5**, 129 (2009).

[29] R. Dronyak *et al*., Appl. Phys. Lett. **95**, 111908 (2009).

[30] H. N. Chapman *et al*., Nat. Phys. **2**, 839 (2006).

[31] A. Barty *et al*., Nature Photon. **2**, 415 (2008).

[32] A. P. Mancuso *et al*., Phys. Rev. Lett. **102**, 035502 (2009).

[33] R. L. Sandberg *et al*., Phys. Rev. Lett. **99**, 098103 (2007).

[34]R. L. Sandberg *et al*., Proc. Natl. Acad. Sci. USA **105**, 24 (2008).
[35]A. Ravasio *et al*., Phys. Rev. Lett. **103**, 028104 (2009).
[36]J. Miao, D. Sayre, and H. N. Chapman, J. Opt. Soc. Am. A **15**, 1662 (1998).
[37]J. R. Fienup, Appl. Opt. **21**, 2758 (1982).
[38]V. Elser, Acta Crystallogr. Sect. A **59**, 201 (2003).
[39]C. C. Chen, J. Miao, C. W. Wang, and T. K. Lee, Phys. Rev. B **76**, 064113 (2007).
[40]S. Marchesini, Rev. Sci. Instrum. **78**, 011301 (2007).
[41]H. H. Bauschke, P. L. Combettes, and D. R. Luke, J. Opt. Soc. Am. A **19**, 1334 (2002).
[42]K. S. Raines *et al*., Nature (London) **463**, 214 (2010).
[43]H. Jiang *et al*., Natl. Acad. Sci. USA **107**, 11234 (2010).
[44]M. R. Howells *et al*., J. Electron Spectrosc. Relat. Phenom. **170**, 4 (2009).
[45]Q. Shen, I. Bazarov, and P. Thibault, J. Synchrotron Radiat. **11**, 432 (2004).
[46]J. Miao, F. Forster, and O. Levi, Phys. Rev. B **72**, 052103 (2005).
[47]E. Lee *et al*., Struct. Biol. **164**, 221 (2008).
[48]Y. Mao, B. P. Fahimian, S. J. Osher, and J. Miao, IEEE Trans. Image Processing **19**, 1259 (2010).
[49]B. P. Fahimian, Y. Mao, P. Cloetens, and J. Miao, Phys. Med. Biol. **55**, 5383 (2010).
[50]C. C. Chen, J. Miao, and T. K. Lee, Phys. Rev. B **79**, 052102 (2009).
[51]A. Averbuch, R. R. Coifman, D. L. Donoho, M. Israeli, and Y. Shkolnisky, SIAM J. Sci. Comput. **30**, 785 (2008).
[52]Y. Takahashi *et al*., Nano Lett. **10**, 1922 (2010).